

Hydrogen Photoproduction from Ethanol–Water Mixtures Over Au–Cu Alloy Nanoparticles Supported on TiO₂

Eduard Bonmatí · Albert Casanovas ·
Inma Angurell · Jordi Llorca

Published online: 17 December 2014
© Springer Science+Business Media New York 2014

Abstract Au/TiO₂, Au_{0.75}Cu_{0.25}/TiO₂, Au_{0.5}Cu_{0.5}/TiO₂ and Au_{0.25}Cu_{0.75}/TiO₂ photocatalysts prepared from preformed Au and Au–Cu alloy nanoparticles of controlled composition and size were loaded over ceramic honeycombs (2 mg cm⁻²) and tested in an optical fiber photoreactor illuminated with UV LEDs (2.6 mW cm⁻²) to continuously produce hydrogen from water and ethanol mixtures in gas phase at $W/F = 4 \text{ g min L}^{-1}$ and 298 K (where W is the weight of the catalyst and F is the flow rate). The photocatalytic honeycombs were characterized by high resolution transmission electron microscopy, high-angle annular dark-field imaging, energy dispersive X-ray, X-ray photoelectron spectroscopy, and UV–Vis spectroscopy. The yield of hydrogen generation was Au_{0.75}Cu_{0.25}/TiO₂ > Au_{0.5}Cu_{0.5}/TiO₂ ~ Au/TiO₂ > Au_{0.25}Cu_{0.75}/TiO₂ ≫ bare TiO₂, thus demonstrating that the addition of small quantities of copper to conventional TiO₂-supported gold photocatalysts promotes the photocatalytic activity, likely by providing effective charge transfer between Au and Cu in the alloy nanoparticles.

Keywords Photocatalysis · Hydrogen · Ethanol · Gold · Copper · Titania

1 Introduction

The direct production of hydrogen from water and sunlight under ambient conditions is certainly one of the most desired routes to generate hydrogen as an energy carrier since it is based on the Sun, which is a perpetual source of energy, and it is an environmentally safe technology. The photocatalytic process is based on electron–hole pairs that are generated in semiconductors upon bandgap excitation by light. Depending on the excitation lifetime relative to that of charge recombination a net fraction of photocharges are present, which are trapped at defect sites or migrate toward the photocatalyst surface. These surface electrons and holes can reduce and oxidize surface adsorbed molecules, respectively. Incorporating organics such as alcohols as sacrificial electron donors into the photocatalytic process increase charge-separation efficiency and give higher H₂ generation rates [1, 2]. The rate of hydrogen evolution is much higher, compared to that obtained in the absence of organics in the irradiated photocatalyst, due to the irreversible oxidation of the organic molecule with photogenerated holes and the concomitant suppression of electron–hole recombination. The use of bio-ethanol as sacrificial agent is particularly appealing since it can be produced renewably from biomass and industrial effluents, it is widely available and it is easy to implement [3, 4]. Using organic wastes and industrial pollutants as sacrificial reagents is highly beneficial because the photoproduction of hydrogen and decomposition of pollutants take place simultaneously.

Another strategy to increase the hydrogen production rate of the photocatalytic process is to add transition metal oxides and noble metal nanoparticles to the semiconductor (cocatalyst) [5]. In particular, deposition of Pt, Au, Pd and Ag nanoparticles onto TiO₂ is well established and has been found to enhance hydrogen photoproduction from

E. Bonmatí · A. Casanovas · J. Llorca (✉)
Institut de Tècniques Energètiques and Centre for Research in NanoEngineering, Universitat Politècnica de Catalunya, Av. Diagonal 647, Ed. ETSEIB, 08028 Barcelona, Spain
e-mail: jordi.llorca@upc.edu

I. Angurell
Departament de Química Inorgànica, Universitat de Barcelona, Martí i Franquès 1, 08028 Barcelona, Spain

alcohol–water mixtures by facilitating electron transfer and therefore inhibiting electron–hole recombination [6–8]. An alternative pathway recently proposed does not involve electron transfer to the metal but the recombination of the hydrogen atoms on the metal (reverse hydrogen spillover) made via the reduction of protons on the surface of TiO₂ [9]. In addition, metal nanoparticles can influence the intrinsic properties of TiO₂ and extend its photoresponse into the visible region of the spectrum [10]. The drawback, however, is the high costs incurred by the use of noble metals. For this reason, increasing attention has been devoted to Cu/Cu₂O/CuO nanoparticles dispersed on TiO₂ [11–25] to attain a cost-effective photocatalyst. Copper species with smaller bandgap and higher work function than bare TiO₂ facilitates light harvesting and charge carrier separation in Cu/TiO₂. Accumulation of electrons enables the Cu species to act as proton reduction sites and enhance the production of hydrogen [26]. Nevertheless, the different performance of Cu species (CuO vs. Cu₂O vs. metallic Cu) is not clear. Even if Cu oxides seem more effective to receive electrons from TiO₂ as compared to metallic Cu, there is clear evidence of reduction of oxidized Cu to form metallic Cu by excited electrons during the photoreaction [27, 28]. Recently, co-modification by both Au and Cu has proven to be more effective than Au/TiO₂ and Cu/TiO₂ for the photocatalytic decomposition of 2-propanol to acetone [29], thus suggesting that the Au–Cu combination might be of interest for the photoproduction of hydrogen as well.

In this work, we test for the first time the performance of Au–Cu alloy nanoparticles with different composition supported over TiO₂ for the production of hydrogen from water, using ethanol as a sacrificial agent. We have grafted a variety of well-defined Au–Cu alloy nanoparticles with different composition on titania from dodecanethiol-capped nanoparticles. In contrast to impregnation and precipitation methods, which are very simple but normally suffer from precise particle size control and can hardly be employed to prepare alloy nanoparticles with a defined composition, organic capping produce size-controlled metal nanoparticles whose particle size and composition is established before deposition on the metal oxide support [30, 31]. Herein the effect of alloying between Au and Cu (metallic) on the photoproduction of hydrogen is unambiguously determined.

2 Experimental Section

2.1 Photocatalyst Preparation

Cordierite (Al₄Mg₂Si₅O₁₈) honeycombs (Rauschert, 100 cells per square inch, pore volume $210 \pm 30 \text{ mm}^3 \text{ g}^{-1}$,

average pore diameter $3 \pm 1.5 \text{ }\mu\text{m}$) measuring 16 mm in diameter and 20 mm length were used as a physical support. They contained exactly 21 square channels with 2.1 mm channel width. The preparation of the Au–Cu/TiO₂ photocatalytic monoliths involved two steps. First, the honeycombs were coated with a pure and perfectly homogeneous TiO₂ layer by soaking them into pure titanium isopropoxide, Ti(OCH(CH₃)₂)₄. The excess of titania precursor was blow with dry air and honeycombs were dried under continuous rotation for 30 min at room temperature followed by 30 min at 393 K and finally calcined at 723 K for 4 h (10 K min^{-1}). The BET surface area of the TiO₂ support was $41 \pm 6 \text{ m}^2 \text{ g}^{-1}$. X-ray diffraction (XRD) showed the presence of both anatase and rutile with a ratio of anatase:rutile $\sim 93:7$. Titania mass was monitored by weight gain and was between 79 and 90 mg, which corresponds to a catalyst loading of about 2 mg cm^{-2} and a photocatalyst layer thickness of about $2 \text{ }\mu\text{m}$. This titania loading was selected to attain an optimal light penetration and to operate in a non-diffusion-limited regime, as discussed in detail in [32].

On the other hand, bimetallic Au–Cu nanoparticles with Au:Cu atomic ratios of 3:1, 1:1, and 1:3 as well as monometallic Au nanoparticles encapsulated with dodecanethiol monolayer shells were synthesized following the two-phase method described for the synthesis of dodecanethiol-capped monometallic Au nanoparticles [33, 34] and metal alloy clusters [35]. AuCl₄[−] and Cu²⁺ species were first transferred from aqueous HAuCl₄ and Cu(NO₃)₂ solutions (30 mM) to toluene solution using tetraoctylammonium bromide as a phase transfer reagent. Dodecanethiol was then added to the solution at a molar ratio of dodecanethiol:(Au + Cu) = 3:2, and an excess of aqueous NaBH₄ was slowly added to reduce the metal salts.

The resulting dodecanethiol-capped metallic nanoparticles were dried and cleaned using ethanol. The nanoparticles were then dissolved in toluene and impregnated onto the honeycombs loaded with TiO₂ by incipient wetness impregnation. The nominal Au loading was 1 wt% with respect to TiO₂. Honeycombs were finally calcined at 673 K for 2 h (2 K min^{-1}) to eliminate the organic shell and to assure a tight contact between the nanoparticles and the TiO₂ support while maintaining their metallic character. This temperature was selected following the study reported in [32]. No further activation was required for the photocatalytic experiments.

2.2 Photocatalyst Characterization

High resolution transmission electron microscopy (HRTEM) was carried out using a JEOL JEM 2010F electron microscope equipped with a field emission source at an accelerating voltage of 200 kV. For the thiol-capped

nanoparticles, the sols were directly dropped onto carbon-coated grids. For the Au–Cu/TiO₂ photocatalysts, powders were suspended in methanol under ultrasonic treatment before they were deposited on holey carbon-coated grids. The point-to-point resolution achieved was 0.19 nm and the resolution between lines was 0.14 nm. A minimum of 250 particles were measured in each sample for particle size determination. The size limit for the detection of nanoparticles on the support was about 1 nm. The average particle diameter was calculated from the mean diameter frequency distribution with the formula: $d = \sum n_i d_i / \sum n_i$, where n_i is the number of particles with particle diameter d_i in a certain range. High-angle annular dark-field imaging (HAADF) and energy dispersive X-ray (EDX) spectroscopy studies were carried out with a Tecnai G2 F20 S-TWIN transmission electron microscope equipped with a field emission electron source operated at 200 kV with a point-to-point resolution of 0.24 nm. X-ray photoelectron spectroscopy (XPS) was performed on a SPECS system equipped with an Al anode XR50 source operating at 150 mW and a Phoibos 150 MCD-9 detector. The pass energy of the hemispherical analyzer was set at 25 eV and the energy step was set at 0.1 eV. Charge stabilization was achieved by using a SPECS Flood Gun FG 15/40. The binding energy (BE) values were referred to the C 1s peak at 284.8 eV. UV–Vis spectra were collected with a Shimadzu UV3600 UV–Vis–NIR spectrometer equipped with an integrating sphere.

2.3 Photoreaction Experiments

We have used an optical fiber honeycomb reactor to combine the immobilization of the photocatalyst with an optimum photon delivery and mass transfer simultaneously as well as scale-up potential, which has been already described in detail in [32, 36]. The light source consists of four high efficiency UV LEDs emitting at a wavelength of 365 ± 5 nm (12 W, 0.7 A) coupled to a bunch of optical fibers (Fig. 1). The optical fibers are made of PMMA [poly(methyl methacrylate)] and measure 0.8 mm in diameter. The fibers were originally coated to avoid light losses, so they were treated individually to obtain lateral irradiation exactly where the monoliths were placed. To attain uniform illumination, the end of the optical fibers was capped with a zinc-based paint to attain back-reflection of light. The photoreactor casing is made of glass and consists of two pieces sealed by an O-ring that allows an easy exchange of the photocatalytic honeycombs. The nominal distance between the surface of the fibers and the walls of the honeycombs is 0.9 ± 0.2 mm. Photoreactions were carried out in gas phase at 298 K in continuous mode at $W/F = 4$ g min L⁻¹. Ethanol:water gaseous mixtures of 100:0, 50:50, 10:90, and 1:99 on a molar basis were

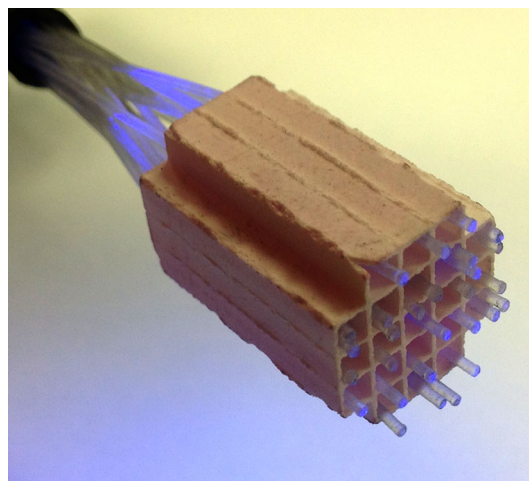


Fig. 1 Photograph of the optical fibers inside the photocatalytic honeycomb

introduced into the photoreactor by bubbling Ar through saturators. The photoreactor effluent was monitored on-line every 1.5 min by gas chromatography (Agilent 3000 A MicroGC) using MS 5 Å, Plot U and Stabilwax columns. Light irradiation was measured directly with a UV-A radiation monitor from Solar Light Co. before and after each photocatalytic test and was 2.60 ± 0.05 mW cm⁻². Blank experiments were carried out with the cordierite monolith support and no photoactivity was measured.

3 Results and Discussion

3.1 Characterization of Photocatalysts

The monometallic Au and Au–Cu alloy nanoparticles as prepared were characterized by HRTEM in order to determine their composition and dimensions. Homogeneous and well-dispersed particles were obtained in all cases with narrow size distributions centered at 3.1–3.3 nm and exhibiting lattice fringes corresponding to single face-centered centered cubic (fcc) phases. On the basis of the phase diagram, Au and Cu form a complete solid solution. Lattice constant values were comprised between those of pure bulk phases of gold ($a_{\text{Au}} = 0.4079$ nm) and copper ($a_{\text{Cu}} = 0.3615$ nm), demonstrating that Au_xCu_{1-x} intermetallic alloys were formed. From the Fourier Transform images corresponding to the lattice fringes in the HRTEM images a precise determination of the lattice parameters and composition of the different Au–Cu alloy nanoparticles was accomplished (Table 1), which were in agreement to the nominal values and Vegard's law [$a_{\text{alloy}} = xa_{\text{Au}} + (1 - x)a_{\text{Cu}} + 0.01198x(1 - x)$] [37].

The same lattice parameters were encountered after deposition of the metal nanoparticles over the TiO₂

support, although their size increased slightly up to 3.8–4.0 nm as a result of the calcination treatment. Nevertheless, a narrow size distribution in each case was maintained (Table 1). Figure 2a shows a representative HRTEM image recorded over the $\text{Au}_{0.75}\text{Cu}_{0.25}/\text{TiO}_2$ photocatalyst. Lattice fringes of the TiO_2 support at 3.52 Å correspond to the (101) crystallographic planes of anatase. In all samples, both anatase and rutile crystallites of about 30–45 nm were encountered, in accordance to XRD (Sect. 2.1). Au–Cu alloy nanoparticles are easily identified in the HRTEM images given their higher electron contrast and lattice fringes (Fig. 2a). The alloy nanoparticles are perfectly crystalline but do not show well-defined facets, which is a consequence of their size and the preparation method employed. Figure 2b shows a representative HAADF image of the $\text{Au}_{0.5}\text{Cu}_{0.5}/\text{TiO}_2$ photocatalyst. The analysis by EDX was systematically performed over individual nanoparticles and, in all cases, a bimetallic nature according to the alloy composition was encountered (Fig. 2c), as expected.

The UV–Vis absorption spectrum of the Au nanoparticles showed the characteristic plasmon resonance band at about 520 nm (Fig. 3a). The band is rather broad, according to the presence of Au nanoparticles of ca. 3 nm [38]. Interestingly, the addition of Cu to form $\text{Au}_{0.75}\text{Cu}_{0.25}$ alloy nanoparticles resulted in an even broader and asymmetric absorption band. To reliably determine the plasmon resonance frequency, we fitted the experimental spectra to a high-order polynomial and defined the plasmon resonance frequency as the zero point of the derivative. In this way, no significant shift of the plasmon band was determined (523 vs. 524 nm for Au and $\text{Au}_{0.75}\text{Cu}_{0.25}$ alloy, respectively), which is in accordance to [39]. The absence of a large absorption band between 400 and 800 nm ascribed to oxidized Cu species [11, 19, 20, 26] indicated that Cu was alloyed with Au in a metallic state, in accordance to HRTEM analysis. When the amount of Cu in the alloy nanoparticles was higher, $\text{Au}_{0.5}\text{Cu}_{0.5}$ and $\text{Au}_{0.25}\text{Cu}_{0.75}$, the plasmon resonance band broadened to an extent that it was no longer visible (Fig. 3a). This increase of peak width in the Au–Cu system has been already reported in the

literature and has ascribed to the larger interband contributions of Cu when compared to those of Au [39, 40].

The UV–Vis absorbance spectra of the Au and Au–Cu alloy nanoparticles after deposition onto TiO_2 and calcination are shown in Fig. 3b. All photocatalysts showed intense absorption below ca. 400 nm due to the TiO_2 support. Photocatalysts Au/TiO_2 , $\text{Au}_{0.75}\text{Cu}_{0.25}/\text{TiO}_2$ and $\text{Au}_{0.5}\text{Cu}_{0.5}/\text{TiO}_2$ exhibited a broad absorption feature at about 560 nm, which is assigned to the localized surface plasmon resonance of the metal nanoparticles supported on TiO_2 , according to literature data [7, 32]. The position of the band blue-shifted slightly as the amount of Cu in the alloy nanoparticles increased. The intensity of the surface plasmon resonance band was less intense in photocatalyst $\text{Au}_{0.25}\text{Cu}_{0.75}/\text{TiO}_2$, although light absorption at 400–600 nm was still more intense with respect to the bare TiO_2 support. The bandgap energies of the photocatalysts were determined from the Tauc plot [19]. The extrapolated bandgap energies for all the samples were very similar, 2.92 ± 0.02 eV. Comparable values have been reported for Au/TiO_2 [7] and Cu/TiO_2 [19] samples.

X-ray photoelectron spectroscopy (XPS) was used to investigate the oxidation states of Au and Cu and the elemental surface composition of Au and Au–Cu alloy nanoparticles following deposition on the cordierite honeycombs loaded with TiO_2 and calcination (Table 2). The Au 4f core-level spectra showed photoemitted electrons with binding energies at 84.0–84.4 eV (Au 4f_{7/2}) indicating that metallic Au was the only gold species on the near surface region of the photocatalysts. The progressive increase in binding energy values observed as the amount of Cu increases in the alloy nanoparticles in an additional indication of the existence of Au–Cu alloys and electron density transfer between copper and gold [31, 40]. The position of the Cu 2p_{3/2} signal in the bimetallic photocatalysts was maintained approximately constant at 933.6–933.7 eV, which is slightly higher than that corresponding to metallic Cu. As regards surface atomic ratios, there is a good correlation between Au/Ti and Cu/Ti values and the respective Au and Cu contents of the photocatalysts (Table 2).

Table 1 Composition and metal particle size distribution (in nm) of nanoparticles as prepared and after deposition on TiO_2 determined by HRTEM

Photocatalyst	Precursor nanoparticles	Supported nanoparticles	Lattice constant	Alloy composition
Au/TiO_2	3.1 (2.5–3.4)	3.8 (3.5–4.3)	0.4077	Au_{100}
$\text{Au}_{0.75}\text{Cu}_{0.25}/\text{TiO}_2$	3.2 (2.7–3.5)	3.8 (3.7–4.5)	0.3973	$\text{Au}_{77}\text{Cu}_{23}$
$\text{Au}_{0.5}\text{Cu}_{0.5}/\text{TiO}_2$	3.3 (2.9–3.6)	4.0 (3.5–4.6)	0.3867	$\text{Au}_{54}\text{Cu}_{46}$
$\text{Au}_{0.25}\text{Cu}_{0.75}/\text{TiO}_2$	3.2 (2.6–3.5)	3.9 (3.6–4.4)	0.3742	$\text{Au}_{27}\text{Cu}_{73}$

Values in parenthesis indicate the range of particle size corresponding to 95 % of all particles. Alloy composition calculated from the lattice constant (in nm) using d_{111} and d_{200} interplanar distances

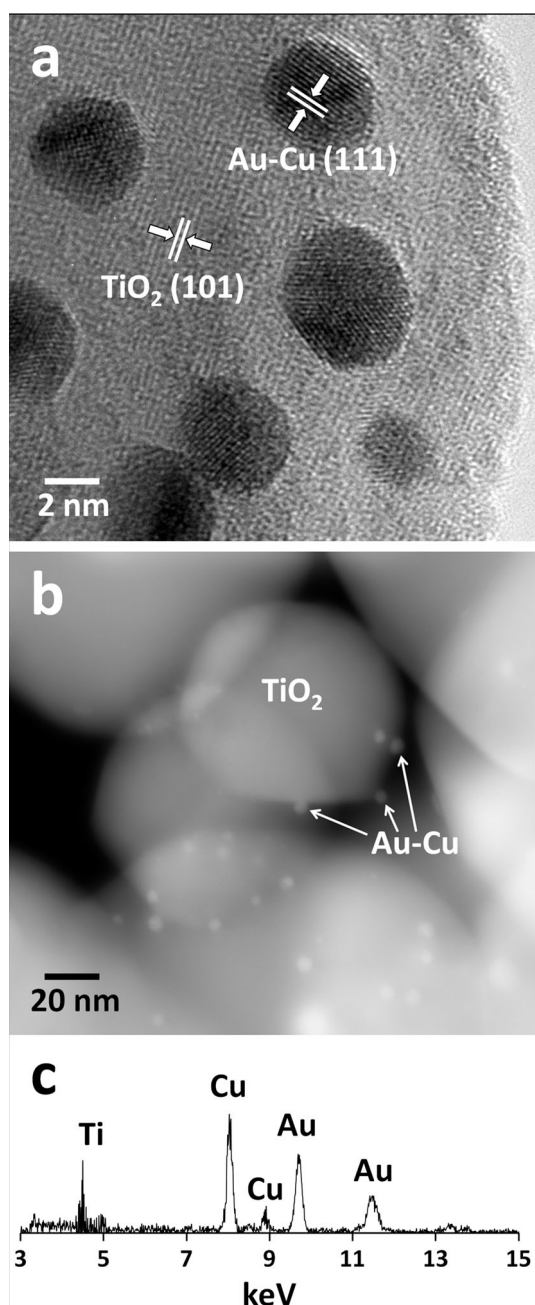


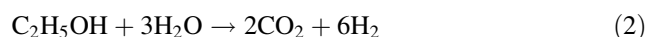
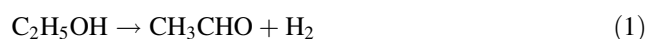
Fig. 2 **a** HRTEM image of the $\text{Au}_{0.75}\text{Cu}_{0.25}/\text{TiO}_2$ photocatalyst, **b** HAADF image of the $\text{Au}_{0.5}\text{Cu}_{0.5}/\text{TiO}_2$ photocatalyst, **c** EDX spectrum of a single Au–Cu particle in the $\text{Au}_{0.5}\text{Cu}_{0.5}/\text{TiO}_2$ photocatalyst

3.2 Photocatalytic Tests

In all the experiments, when the light was turned on after purging the system, immediately the photoproduction of H_2 started and shortly after steady state was reached. By using a sweep gas flow (Ar) of 20 mL min^{-1} the concentration of H_2 in the outlet stream oscillated between 0.01 and 0.08 % depending on the photocatalyst and the

ethanol–water mixture employed. The photoproduction of H_2 was maintained constant independently on the sweep gas flow used, thus assuring the absence of diffusion limitations under the operational conditions tested. From now onwards, only the photoproduction rates normalized to the photocatalyst weight and the UV intensity reaching the honeycomb walls ($\text{mmol h}^{-1} \text{g}_{\text{cat}}^{-1} \text{W}^{-1}$) will be considered, which are independent of the sweep gas flow used. The only products detected at the reactor outlet were hydrogen, acetaldehyde, carbon dioxide, and trace amounts of dimethyl ketone. A blank experiment with a honeycomb loaded only with TiO_2 did not show appreciable hydrogen photoproduction.

Figure 4 shows the photoproduction rates at steady state of hydrogen, acetaldehyde and carbon dioxide obtained over the photocatalysts tested under different ethanol–water mixtures. The values shown for each experiment and the error bars correspond to the average of eight measurements. In all cases, the major products of the reaction were H_2 and acetaldehyde, in accordance to previous reports [32, 36] and Eq. (1).



It is observed that the photoproduction of hydrogen was, in all cases, higher than that of acetaldehyde, which means that other photoreactions operated as well, although the partial adsorption of acetaldehyde onto the photocatalyst cannot be completely ruled out [32]. In any case, the differences among the amount of H_2 with respect to that of acetaldehyde were maintained approximately constant for the ethanol:water mixtures containing 10, 50 and 100 % ethanol, irrespectively of the photocatalyst and the production rates. In contrast, for the more diluted ethanol concentration (1 % ethanol) the photoproduction of H_2 was considerably higher than that of acetaldehyde and, at the same time, the amount of CO_2 produced increased considerably. The formation of CO_2 can be explained in terms of ethanol reforming with water (Eq. 2), which is favored under high water partial pressure. The mass balance calculations ($[\text{H}_2] \sim [\text{CH}_3\text{CHO}] + 3[\text{CO}_2]$) were consistent with this scheme of reactions. Finally, the appearance of trace amounts of dimethyl ketone can be explained by the reaction of acetaldehyde with water (Eq. 3).



For all photocatalysts it was clearly observed that the higher the ethanol content in the reaction mixture the higher the H_2 photoproduction rate. This has been already reported in the literature [32, 36] and has been related to a beneficial effect of alcohol concentration on hole scavenging on TiO_2 .

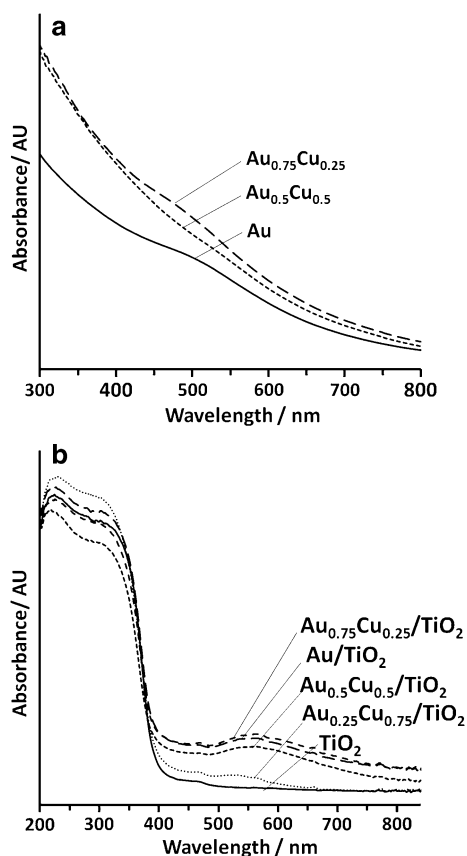


Fig. 3 UV–Vis absorbance spectra of **a** Au, $\text{Au}_{0.75}\text{Cu}_{0.25}$ and $\text{Au}_{0.5}\text{Cu}_{0.5}$ alloy nanoparticles in toluene and of **b** nanoparticles supported over TiO_2 (photocatalytic honeycombs)

Table 2 Binding energies (BE, in eV) and surface atomic ratios determined by XPS

Photocatalyst	BE Au	BE Cu	Au/Ti	Cu/Ti	Au/ Cu
	4f _{7/2}	2p _{3/2}			
Au/TiO ₂	84.0	–	0.0038	–	–
$\text{Au}_{0.75}\text{Cu}_{0.25}/\text{TiO}_2$	84.1	933.6	0.0035	0.0015	2.3
$\text{Au}_{0.5}\text{Cu}_{0.5}/\text{TiO}_2$	84.1	933.6	0.0043	0.0071	0.6
$\text{Au}_{0.25}\text{Cu}_{0.75}/\text{TiO}_2$	84.4	933.7	0.0054	0.0173	0.3

Concerning the H_2 photoproduction rates obtained over the different photocatalysts, it is clear from Fig. 4 that, for each condition, the amount of H_2 produced followed the trend: $\text{Au}_{0.75}\text{Cu}_{0.25}/\text{TiO}_2 > \text{Au}_{0.5}\text{Cu}_{0.5}/\text{TiO}_2 \sim \text{Au}/\text{TiO}_2 > \text{Au}_{0.25}\text{Cu}_{0.75}/\text{TiO}_2$. Therefore, the H_2 photoproduction rate is enhanced in absolute terms when Cu is alloyed with Au up to a Au:Cu ratio of 1:1. In particular, the photoproduction rates of hydrogen recorded over the $\text{Au}_{0.75}\text{Cu}_{0.25}/\text{TiO}_2$ photocatalyst were about 50 % higher than those obtained over the standard Au/TiO₂ photocatalyst. Taking into account that the amount of Au is lower in this photocatalyst, the photoproduction of H_2 over $\text{Au}_{0.75}\text{Cu}_{0.25}/\text{TiO}_2$ is significantly higher than that obtained over Au/TiO₂ on a gold content basis.

Since no appreciable bandgap differences are measured by UV–Vis absorption spectroscopy upon alloying Au with Cu, the reason for the enhancement of hydrogen production is likely the electron transfer between Au and Cu in the alloy nanoparticles, as deduced from XPS, which would diminish the recombination rate between photogenerated electrons and holes in TiO_2 . Recently, time resolved microwave conductivity measurements for Au–Cu alloy nanoparticles supported on TiO_2 used for phenol photodegradation have demonstrated improved efficiency in electron scavenging than the monometallic Au and Cu counterparts [41]. Unfortunately, to the best of our knowledge no hydrogen recombination data has been reported for Au–Cu alloys compared to Au, so it is not possible to discuss the alternative view recently appeared in [9] concerning the role of the metal cocatalysts as a recombination centers to yield the final molecular H_2 product from reduced hydrogen atoms generated on TiO_2 .

Figure 5 shows the photoproduction rates of H_2 obtained over the different photocatalysts (EtOH:H₂O = 1:10 molar) normalized to the surface area of Au and to the total metal surface area (Au + Cu). For this calculation it has been taken into account the weight of catalyst in each photocatalytic honeycomb, the theoretical surface composition of the alloy, the particle size of the nanoparticles recorded by HRTEM (Table 1), and the Au/Ti surface atomic ratio obtained by XPS (Table 2). The amount of H_2 produced normalized to the calculated Au surface area follows the trend: $\text{Au}_{0.75}\text{Cu}_{0.25}/\text{TiO}_2 > \text{Au}_{0.5}\text{Cu}_{0.5}/\text{TiO}_2 > \text{Au}/\text{TiO}_2 > \text{Au}_{0.25}\text{Cu}_{0.75}/\text{TiO}_2$, whereas the amount of H_2 produced normalized to total metal (Au + Cu) surface area follows the trend: $\text{Au}_{0.75}\text{Cu}_{0.25}/\text{TiO}_2 > \text{Au}/\text{TiO}_2 > \text{Au}_{0.5}\text{Cu}_{0.5}/\text{TiO}_2 > \text{Au}_{0.25}\text{Cu}_{0.75}/\text{TiO}_2$. It is therefore concluded that the addition of small amounts of Cu to Au/TiO₂ is beneficial for the photoproduction of hydrogen and can be viewed as a simple strategy to decrease the photocatalyst cost.

The apparent quantum efficiency (AQE) for hydrogen photogeneration was calculated from the ratio of the double amount of H_2 (r_{H_2}) and the overall amount of photons irradiated by the optical fibers (N_λ) using the equation $\text{AQE} = (2 \times r_{\text{H}_2}/N_\lambda) \times 100$ and assuming optimal light absorption, operation in a non-diffusion-limited regime, and that two photons were required for liberation of one hydrogen molecule. The AQE values obtained with the $\text{Au}_{0.75}\text{Cu}_{0.25}/\text{TiO}_2$ photocatalyst using 1, 10, 50 and 100 % ethanol in water were 8.9, 9.5, 12.6 and 16.9 %, respectively.

4 Conclusions

Au–Cu/TiO₂ photocatalysts were prepared from pre-formed Au and Au–Cu alloy nanoparticles, characterized

Fig. 4 Photoproduction rates of hydrogen, carbon dioxide and acetaldehyde over the photocatalytic honeycombs tested using different ethanol–water mixtures

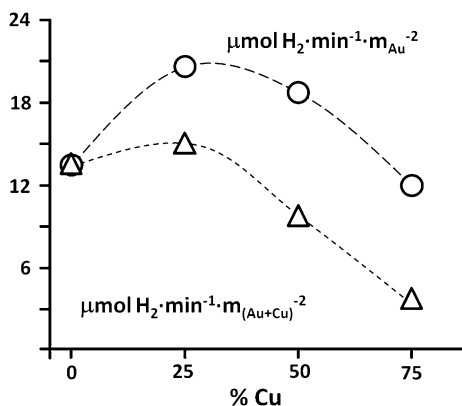
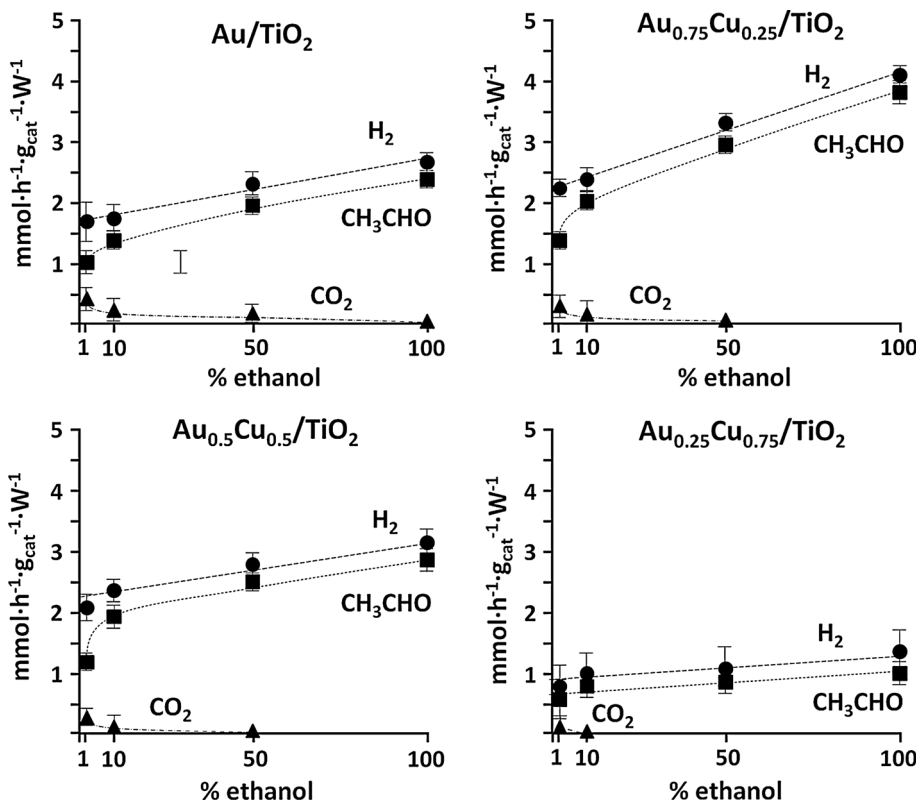


Fig. 5 Hydrogen photoproduction rates normalized to Au surface area (open circle) and to Au + Cu surface area (open triangle) for the different photocatalytic honeycombs tested with a molar ethanol:water ratio of 1:10

by UV–Vis spectroscopy, HRTEM, HAADF, EDX and XPS, loaded onto catalytic walls (cordierite honeycombs), and tested in an optical fiber photoreactor for the photoproduction of hydrogen from various water–ethanol mixtures. The Au and Au–Cu alloy nanoparticles measured about 3 nm as prepared and about 4 nm after deposition and calcination over the photocatalytic honeycombs loaded with the TiO₂ support. HRTEM was used to calculate the

lattice parameters of the Au–Cu alloy nanoparticles and EDX to corroborate their bimetallic nature. Plasmon resonance bands at about 520 nm were identified for the Au, Au_{0.75}Cu_{0.25} and Au_{0.5}Cu_{0.5} nanoparticles as prepared, whereas localized surface plasmon resonance of the metal nanoparticles supported on TiO₂ were visible in the UV–Vis absorbance spectra for all samples at about 560 nm. No bandgap differences were observed in the photocatalysts containing Au–Cu alloy nanoparticles. XP spectra showed Au and Cu in metallic state in all cases, and a progressive shift in the Au 4f signal towards higher binding energies as the amount of Cu increased in the photocatalyst, indicating electron density transfer between copper and gold. This electron transfer is considered responsible for the hydrogen enhancement measured over the Au–Cu/TiO₂ photocatalysts. The yield of hydrogen generation was Au_{0.75}Cu_{0.25}/TiO₂ > Au_{0.5}Cu_{0.5}/TiO₂ ~ Au/TiO₂ > Au_{0.25}Cu_{0.75}/TiO₂ ≫ bare TiO₂. The photoproduction rate of hydrogen over Au_{0.75}Cu_{0.25}/TiO₂ was about 50 % higher than that obtained over the standard Au/TiO₂ photocatalyst, both in terms of absolute H₂ as well as the amount of H₂ generated with respect to Au surface area exposed. The partial substitution of Au by Cu in conventional Au/TiO₂ photocatalysts may represent a simple strategy to increase the cost-effectiveness of this type of photocatalysts for producing hydrogen from water–alcohol mixtures.

Acknowledgments This work has been funded through Grant MI-NECO ENE2012-36368. J.L. is Serra Húnter Fellow and is grateful to the ICREA Academia program.

References

1. Kondarides DI, Daskalaki VM, Patsoura A, Verykios XE (2008) *Catal Lett* 122:26–32
2. Nadeem MA, Murdoch M, Waterhouse GIN, Metson JB, Keane MA, Llorca J, Idriss H (2010) *J Photochem Photobiol A* 216:250–255
3. Llorca J, Cortés V, Divins NJ, Olivera R, Taboada E (2013) In: Gandía LM, Arzamendi G, Diéguez PM (eds) *Renewable hydrogen technologies*. Elsevier, Amsterdam
4. Idriss H, Scott M, Llorca J, Chan SC, Chiu W, Sheng PY, Yee A, Blackford MA, Pas SJ, Hill AJ, Alamgir FM, Rettew R, Petersburg C, Senanayake S, Barteau MA (2008) *ChemSusChem* 1:905–910
5. Bamwenda GR, Tsubota S, Nakamura T, Haruta M (1995) *J Photochem Photobiol A* 89:177–189
6. Murdoch M, Waterhouse GIN, Nadeem MA, Metson JB, Keane MA, Howe RF, Llorca J, Idriss H (2011) *Nat Chem* 3:489–492
7. Jovic V, Chen WT, Waterhouse DS, Blackford MG, Idriss H, Waterhouse GIN (2013) *J Catal* 305:307–317
8. Waterhouse GIN, Wahab AK, Al-Oufi M, Jovic V, Anjum DH, Sun-Waterhouse D, Llorca J, Idriss H (2013) *Sci Rep* 3:2849
9. Joo JB, Dillon R, Lee I, Yin Y, Bardeen CJ, Zaera F (2014) *PNAS* 111:7942–7947
10. Subramanian V, Wolf E, Kamat PV (2003) *Langmuir* 19:469–474
11. Xu S, Du AJ, Liu J, Ng J, Sun DD (2011) *Int J Hydrogen Energy* 36:6560–6568
12. De Jongh PE, Vanmaekelbergh D, Kelly JJ (1999) *Chem Commun* 12:1069–1070
13. Barreca D, Fornasiero P, Gasparotto A, Gombac V, Maccato C, Montini T, Tondello E (2009) *ChemSusChem* 2:230–233
14. Cheng WY, Yu TH, Chao KJ, Lu SY (2014) *ChemCatChem* 6:293–300
15. Barreca D, Carraro G, Gombac V, Gasparotto A, Maccato C, Fornasiero P, Tondello E (2011) *Adv Funct Mater* 21:2611–2623
16. Montini T, Gombac V, Sordelli L, Delgado JJ, Chen X, Adami G, Fornasiero P (2011) *ChemCatChem* 3:574–577
17. Miwa T, Kaneco S, Katsumara H, Suzuki T, Ohta K, Verma SC, Sugihara K (2010) *Int J Hydrogen Energy* 35:6554–6560
18. Sangpour P, Hashemi F, Moshfegh AZ (2010) *J Phys Chem C* 114:13955–13961
19. Yoong LS, Chong FK, Dutta BK (2009) *Energy* 34:1652–1661
20. Yu J, Hai Y, Jaroniec M (2011) *J Colloid Interface Sci* 357:223–228
21. Choi HJ, Kang M (2007) *Int J Hydrogen Energy* 32:3841–3848
22. Bandara J, Udawatta CP, Rajapakse CS (2005) *Photochem Photobiol Sci* 4:857–861
23. Sreethawong T, Yoshikawa S (2005) *Catal Commun* 6:661–668
24. Jin ZL, Zhang XJ, Li YX, Li SB, Lu GX (2007) *Catal Commun* 8:1267–1273
25. Xu S, Sun DD (2009) *Int J Hydrogen Energy* 34:6096–6104
26. Xu S, Ng J, Zhang X, Bai H, Sun DD (2010) *Int J Hydrogen Energy* 35:5254–5261
27. Wu NL, Lee MS (2004) *Int J Hydrogen Energy* 29:1601–1605
28. Zhang S, Wang H, Yeung M, Fang Y, Yu H, Peng F (2013) *Int J Hydrogen Energy* 38:7241–7245
29. Nogawa T, Isobe T, Matsushita S, Nakajima A (2012) *Mater Lett* 82:174–177
30. Templeton AC, Wuelfing WP, Murray RW (2000) *Acc Chem Res* 33:27–36
31. Llorca J, Domínguez M, Ledesma C, Chimentao RJ, Medina F, Sueiras J, Angurell I, Seco M, Rossell O (2008) *J Catal* 258:187–198
32. Taboada E, Angurell I, Llorca J (2014) *J Catal* 309:460–467
33. Brust M, Walker M, Bethell D, Schiffrin DJ, Whyman R (1994) *J Chem Soc Chem Commun* 7:801–802
34. Kiely CJ, Fink J, Zheng JG, Brust M, Bethell D, Schiffrin D (2000) *J Adv Mater* 12:640–643
35. Hostetler MJ, Zhong CJ, Yen BKH, Anderegg J, Gross SM, Evans ND, Porter M, Murray RW (1998) *J Am Chem Soc* 120:9396–9397
36. Taboada E, Angurell I, Llorca J (2014) *J Photochem Photobiol A* 281:35–39
37. De G, Rao CNR (2003) *J Phys Chem B* 107:13597–13600
38. Su YH, Wang WL (2013) *Nanoscale Res Lett* 8:408–413
39. Motl NE, Ewusi-Annan E, Sines IT, Jensen L, Schaak RE (2010) *J Phys Chem C* 114:19263–19269
40. Kim MJ, Na HJ, Lee KC, Yoo EA, Lee M (2003) *J Mater Chem* 13:1789–1792
41. Hai Z, El Kolli N, Uribe DB, Beaunier P, José-Yacamán M, Vigneron J, Etcheberry A, Sorques S, Colbeau-Justin C, Chen J, Remita H (2013) *J Mater Chem A* 36:10829–10835